



Optical, Magnetic, Dielectric and Antimicrobial Properties of $\text{MnCuFe}_2\text{O}_4$ Nanoparticles

B. Surendra Babu¹, Ramakrishna Rao Bhonsle^{1,*}, D. Baba Basha² , B. Venkata Shiva Reddy³ 

¹. Department of Chemistry, GITAM Deemed to be University, Bangalore, Karnataka 562163, India

². College of Computer and Information Sciences, Majmaah University Al' Majmaah, K.S.A-11952, Saudi Arabia

³. Department of Physics, The National College, Bagepalli, 561207, Karnataka, India

* Correspondence: rbhonsle@gitam.edu

Scopus Author ID 57224275157

Received: 1.12.2023; Accepted: 15.04.2024; Published: 19.07.2024

Abstract: Low-temperature hydrothermal synthesis produced $\text{Mn}_{1-x}\text{Cu}_x\text{Fe}_2\text{O}_4$ ($x = 0.02, 0.04, 0.06,$ and 0.08) (MCF) nanoparticles (NPs). The MCF system produced a cubic spinel, according to X-ray diffraction. The average crystallite size varied from 53.6 to 79.8 nm. In FTIR investigations, broad (ν_1) and narrow (ν_2) absorption bands may indicate cation distributions in tetrahedral and octahedral locations, respectively. The surface morphology was FESEM-analyzed. The dependence of the optical bandgap shift ($E_g \sim 2.250\text{-}2.280$ eV) on substituent concentration was clarified. Magnetization versus applied magnetic field (M-H) loops showed that MCF NPs are superparamagnetic and useful for biological applications. Magnetization against magnetic field (M-H) curves for $x = 0.02, 0.04, 0.06,$ and 0.08 revealed small remanence magnetization (M_r) and coercivity (H_c). This confirmed MCF NPs were superparamagnetic. An antibacterial examination using green-method MCF showed a 10.8 mm zone of inhibition of *Escherichia coli* and 9.4 mm for *Streptococcus pneumoniae*.

Keywords: nanoparticles; morphology; dielectric properties; impedance; antimicrobial.

© 2024 by the authors. This article is an open-access article distributed under the terms and conditions of the Creative Commons Attribution (CC BY) license (<https://creativecommons.org/licenses/by/4.0/>).

1. Introduction

Iron, cobalt, nickel, etc., are only magnetic substances, but it is wrong to think that even paper, glass, wood, and silver are magnetic substances. All available materials are magnetic. Any materials that experience a strong or weak force in the presence of a magnetic field are called magnetic materials. On the basis of behavior, magnetic materials are classified into Diamagnetic, Paramagnetic, Ferromagnetic, Antiferromagnetic, and Ferrimagnetic substances. But, based on the application, these materials are divided into hard and soft magnetic substances. To study the magnetic behavior of materials, some quantities like magnetic induction (\vec{B}), magnetization (\vec{M}), magnetic intensity (\vec{H}), absolute permeability (μ), relative permeability (μ_r), and magnetic susceptibility (χ) are important.

The word ferrite is from Latin, i.e., Ferrum, which means iron. In magnetic materials, the ferrites are the main class of materials in which Fe^{3+} cations' role is prominent in composition. Ferrites have been known to the world since 800 BCE in Greece. In the modern period, in 1928, Forestier came forward to prepare ferrites using the heat treatment method. In 1947, Snoek prepared many ferrites, and in 1950, ferrites were used in television technology as high-voltage transformers and electron deflection yokes. Based on the chemical

composition, magnetic properties, and structure, ferrites are classified into spinels, garnets, hexaferrites, and orthoferrites; these substances exhibit magnetically as soft and hard materials. The magnetic materials of the polycrystalline substances, which are spinel structures, exhibit a versatile role in various domains owing to higher magnitude of permeability, magnetization, minimum values of eddy currents, electrical conductivity, etc. [1-7]. Magnetic spinels are suitable materials for spintronics, resonators, microwave devices, electronics, radio-electronics, phase shifters, filters, EMI shields, etc. [2]. The ferrimagnetic spinels generally have a chemical formula MFe_2O_4 , where M is divalent cations such as Ni, Mg, Cu, Zn, Mn, Co, Ca, etc. [3]. The initial stage of research was limited to the basic spinel structures. However, as time lapsed, the research was extended to adding dopants into the basic structure of spinel ferrites. The main dopants are alkali elements, alkaline metals, transition metals, and rare earth elements. In this context, the researcher emphasized substituting divalent copper with $MnFe_2O_4$, expecting the advanced properties.

In the literature survey, S.A. Mazen *et al.* [4] synthesized “Effect of divalent metal ions substitution on structural and magnetic properties of $Li_{0.25}Mn_{0.5-x}M_xFe_{2.25}O_4$ ($M = Co^{2+}, Ni^{2+}, Cu^{2+}$) spinel ferrites”. The structural analysis by XRD gave a cubic structure for all substitutions of Co^{2+}, Ni^{2+} , and Cu^{2+} , as well as decreasing order lattice parameters with increasing dopant concentration. For $Li_{0.25}Mn_{0.5-x}Co_xFe_{2.25}O_4$ the lattice parameters were varied from 0.842 nm, 0.841 nm, 0.838 nm and 0.836 nm for $x=0.0, 0.1, 0.2, 0.3$ respectively, for $Li_{0.25}Mn_{0.5-x}Ni_xFe_{2.25}O_4$ lattice parameters were 0.840 nm, 0.837 nm and 0.834 nm for $x=0.1, 0.3$ and 0.5 respectively and $Li_{0.25}Mn_{0.5-x}Cu_xFe_{2.25}O_4$ lattice parameters were 0.841 nm, 0.839 nm and 0.837 nm for $x=0.1, 0.3$ and 0.5 respectively. The microstructures of SEM analysis revealed the presence of intergranular porosity and intragranular porosity, which was absent. M.H. Abdellatif *et al.* [5] studied the Crystal field deformation by Ce^{3+} doping in spinel Mn-Cr ferrite, synthesized by standard ceramic technique. The TEM images showed coherent rounded nanoparticles, and the average size of particles was 50 nm. Bajarang B. Patil [6] explained the effect of divalent materials on ferrite structures. In the recent decade, extensive research has been done on adding divalent atoms ($Zn^{2+}, Cu^{2+}, Mn^{2+}, Ni^{2+}, Mg^{2+}$) into the Cu-Ni-Zn ferrite structures. A recent research report showed that Mg^{2+} and Mn^{2+} enhanced the permeability in the Cu-Ni-Zn ferrite structures. In $Ni_{0.4}Cu_{0.3}Zn_{0.3}Ag_{0.4x}Mn_{0.3x}Cr_{0.3x}Fe_{2-x}O_4$ ($x = 0.0, 0.05, 0.10, 0.15$) prepared by the sol-gel method reported the increase of lattice parameters and volume of the unit cell, decrease the dc resistivity, inverse relation between saturation magnetization and coercivity and lower coercivity by nanoferrites materials possess power applications. In a review article by O. Dehghani Dastjerdi *et al.*, a review of synthesis, characterization, and magnetic properties of soft spinel ferrites [7], the crystallographic properties obtained for the $MnFe_2O_4$; crystal structure was cubic (FCC), lattice constant was 8.511 Å, unit cell volume 616.512 Å³ and theoretical density 2.484 g/cc and the magnetic properties were high in the composition of $Co_{0.2}Mn_{0.8}Fe_2O_4$ i.e., H_c value 121.46 Oe, M_r value 15.93 emu/g and M_s 61.69 value emu/g value. Kaliram Patil *et al.* [8] studied structural and dielectric properties of Zn^{2+} doped $MnFe_2O_4$ and $NiFe_2O_4$ spinel ferrites synthesized by solid-state reaction and reported the cubic structure. The lattice parameters of Zn^{2+} doped $MnFe_2O_4$ and $NiFe_2O_4$ spinel ferrites were 8.35 Å and 8.422 Å, respectively. M.D. Hossain *et al.* [9], review in Hysteresis loop properties of rare earth doped spinel ferrites; $Ni_{0.5}Cu_{0.2}Cd_{0.3}La_xFe_{2-x}O_4$ ($X=0.000, 0.015, 0.030, 0.045$ and 0.060) synthesized by sol-gel auto combustion. The M_r/M_s values were 0.07, 0.06, 0.03, 0.04, and 0.08 for their increasing compositions. Abanti Nag *et al.* [10] studied the influence of doping on the magnetic and electromagnetic properties

of spinel ferrites synthesized by the sol-gel auto-combustion route. Mouna El Abboubi *et al.* [11] review on Integration of spinel ferrite magnetic nanoparticles into organic solar cells: a review. Muhammad Zahid *et al.* [12] studied the optimization of nanocrystalline copper-doped spinel ferrites' structural, dielectric, and magnetic properties. Shameran Jamal Salih *et al.* [13] review on magnetic spinel ferrite (MFe_2O_4) nanoparticles: From synthesis to application. Nida Khan *et al.* [14] worked out on sol-gel auto-combustion synthesis and characterization of Nd^{3+} doped $Cu_{0.5}Co_{0.5}Fe_{2-x}Nd_xO_4$ ($x = 0.0, 0.1, 0.2, 0.3, 0.4,$ and 0.5) spinel ferrites; the XRD pattern is shown single phase of cubic structure without any secondary phases. Studied structural, optical, dielectric, and magnetic properties of Nd^{3+} ion-substituted Ni-Mg-Cu spinel ferrites.

In the current research work, we focused on preparing the compound as $Mn_{1-x}Cu_xFe_2O_4$ ($X=0.02, 0.04, 0.06,$ and 0.08) (MCF), and the method adopted was hydrothermal. The reason behind this is to observe the compound's resultant magnetic, dielectric, and thermal behavior in the presence of the Copper element in the ferrite structure. In the preparation process, we adopted the hydrothermal method, which is more economical, takes less time, has good homogeneity with high crystallinity, etc. As a whole, it was observed that no work was done on the compound $Mn_{1-x}Cu_xFe_2O_4$ ($X=0.02, 0.04, 0.06,$ and 0.08) prepared via the hydrothermal method.

2. Materials and Methods

For the synthesis of $Mn_{1-x}Cu_xFe_2O_4$ ($X=0.02, 0.04, 0.06$ and 0.08)/ $MnCuFe_2O_4$ (MCF) nanocomposites, we selected the starting material as Manganese nitrate [$Mn(NO_3)_2 \cdot 4H_2O$ (99.8% purity, Sigma-Aldrich)], Copper nitrate [$Cu(NO_3)_2 \cdot 3H_2O$ (99.8% purity, Sigma-Aldrich)], and Iron nitrate [$Fe(NO_3)_3 \cdot 9H_2O$ (99.8% purity, Sigma-Aldrich)]. The sodium hydroxide (NaOH) pellets and their aqueous solution were also used as catalysts and solvents in hydrothermal reactions.

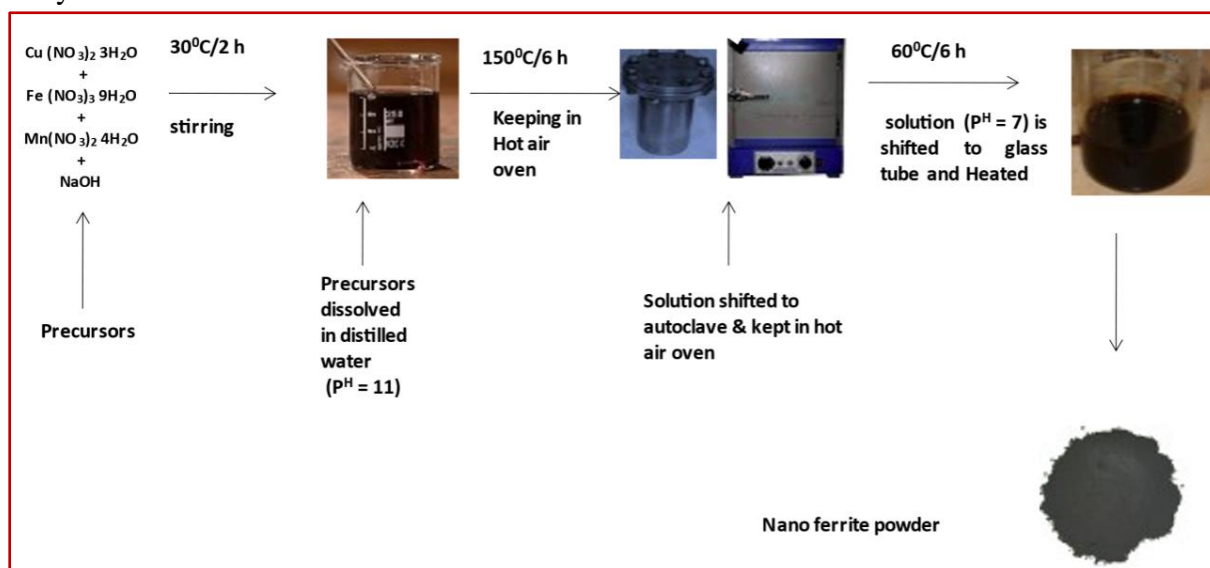


Figure 1. Stepwise schematic representation of MCF.

The precursors are dissolved in distilled water in a ratio of 1:4, and the mixture is stirred constantly at 460 rpm (at $35^\circ C$) to get a homogenous solution. In the middle of the stirring process, the sodium hydroxide solution is poured into the precursor mixture to reach a pH of 11. The resultant solution is shifted to 500 ml of Teflon bowl. Then, the bowl is placed in an autoclave. The autoclave is kept in the oven. The further reaction is executed at $150^\circ C$ /6 hrs. After the reaction, the autoclave is removed from the oven after reaching room temperature.

Slowly, the screws are removed, and the Teflon bowl is opened. Then, the nanoparticles are seen. The water is removed slowly by the injection needle. A level comes when it is impossible to remove small water bits. At this time, the sample is heated at 60°C/6 hrs. Then, the dried sample is ground well in an agate motor. The fine nanoparticle powder samples are subjected to various analysis methods.

The stepwise preparation of the MCF is shown in Figure 1.

3. Results and Discussion

The XRD analysis confirmed the structural parameters and diffraction pattern of MCF, as depicted in Figure 2. The diffraction peaks for X=0.02-0.08 compositions have been noticed, and the (311) reflection plane exhibited the highest intensity peaks. All these diffraction peaks agree with the JCPDS file 77-0100 of CuFe₂O₄. The crystallite of all diffraction peaks was calculated using the Scherrer equation [15], and finally, the average crystallite size values were calculated for all compositions. D_a denotes the average crystallite size, and the values are given in Table 1.

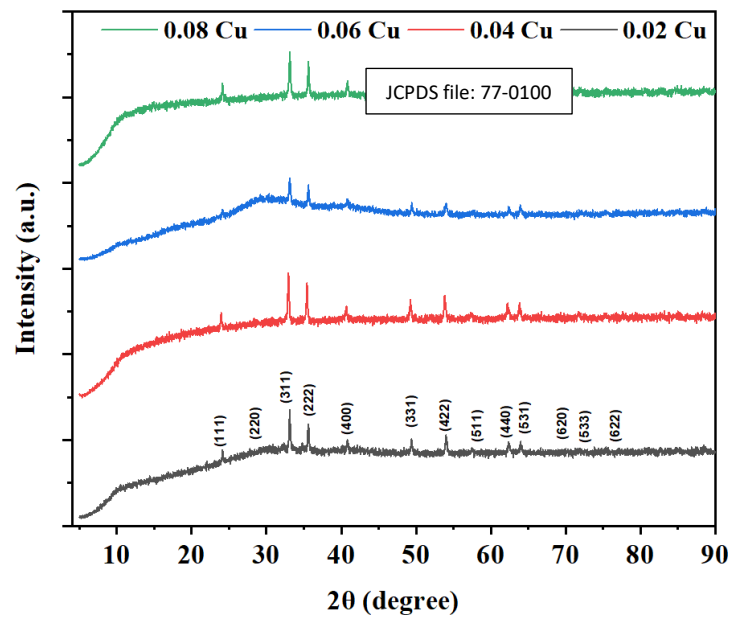


Figure 2. XRD patterns Mn_{1-x}Cu_xFe₂O₄ (X=0.02, 0.04, 0.06 and 0.08) nanoparticles.

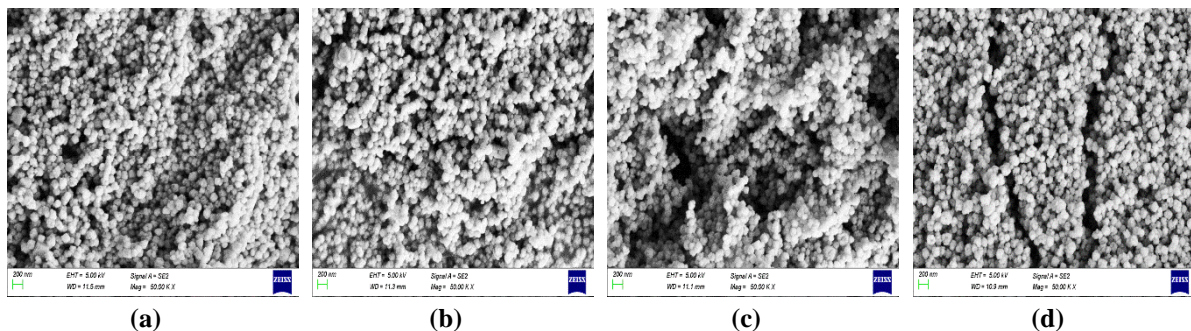


Figure 3. FESEM pictures of Mn_{1-x}Cu_xFe₂O₄ (a) X=0.02; (b) X= 0.04; (c) X= 0.06; (d) X= 0.08 nanoparticles.

The D_a values were neither descending nor ascending order with respect to composition from X=0.02 to X=0.08. However, in the lower composition from X=0.02-0.04 D_a values were

increased from 71.4 to 79.8 nm due to the microstrain decrease during the autoclave chemical reaction. In the higher composition values, i.e., from X=0.06 to 0.08, the D_a values decreased from 77.8 to 53.6 nm due to the microstrain increase during the chemical reaction. This trend of crystallite size variation is common in most ferrites [16-18].

Table 1. Data on XRD parameters of $Mn_{1-x}Cu_xFe_2O_4$ (X=0.02-0.08) nanoparticles.

X	0.02	0.04	0.06	0.08
Da(nm)	71.4	79.8	77.8	53.6
a=b=c (Å)	8.41	8.382	8.354	8.35
V (nm)	594.82	588.9	583.02	582.19
MW (g/mole)	230.800	230.972	231.144	231.316
ρ_x (g/c.c)	5.165	5.217	5.27	5.277
S (m ² /g)	16.3	14.4	14.9	25.7
G (nm)	98.78	104.17	98.09	87.63

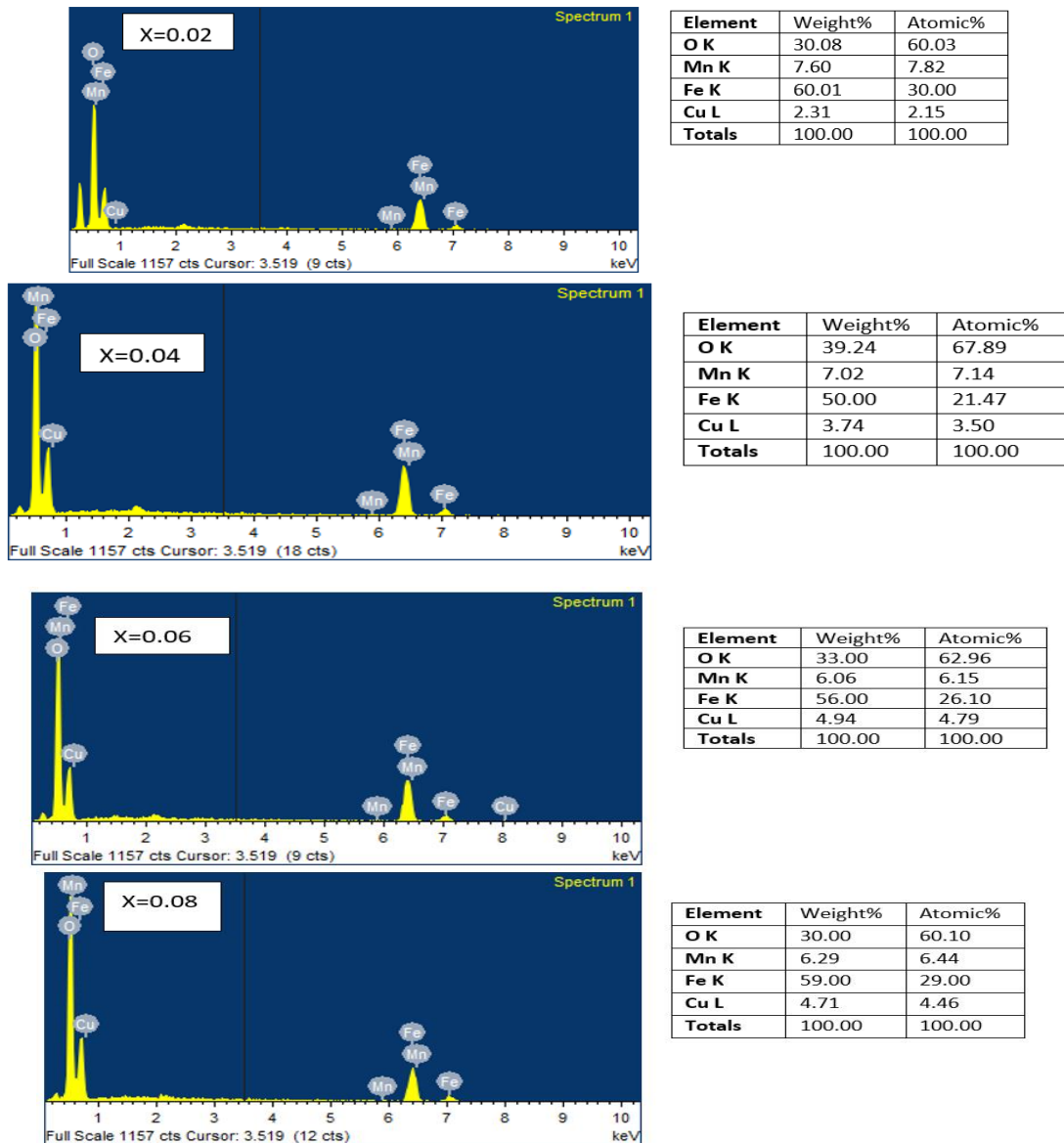


Figure 4. EDAX spectra of MCF nanoparticles.

The lattice constants were decreased from 8.41 to 8.35 Å with Cu content. This trend is attributed to lower ionic radii of Cu^{2+} : 0.73 Å than that of Mn^{2+} : 1.35 Å and Fe^{3+} : 0.645 Å elements present in the compound, as suggested by Shannon [19]. The Cu^{2+} ions are likely to favor occupying the octahedral (B) sites, and Fe^{3+} ions have an equal chance of occupying both sites. Adding Cu cations cannot replace Mn or ferric cations in the ferrite system. Subsequently,

the secondary phases were also noticed. The X-ray density (ρ_x) is calculated and shown in Table 1. These values were increased from 5.165 to 5.277 g/cc as a function of X= 0.02 to 0.08. This type of trend is attributed to the increased molecular weight of the compound from 230.800 to 231.316 g/mole. The reciprocal relationship between crystallite size and specific surface area was noticed. The morphology of the MCF has been studied by the FESEM (Figure 3) with a scale of 200 nm (for X=0.02-0.08), magnification of 50 K, and working distance varied from 10.9 to 11.5 nm. The FESEM pictures clearly indicate that grains are asymmetrical spheres connected due to magnetic interactions. The linear intercept technique was adopted to find the average grain size (G) [20,21], and the values are given in Table 1. The EDAX spectra of MCF nanoparticles of all compositions were recorded in Figure 4. It is evidenced that all the compositions offered quantitative analysis. It implied a fact that all elements, such as oxygen (O), manganese (Mn), copper (Cu), and Iron (Fe), were present without any traces of impurities in the sample.

The band gap or energy gap (e.g.,) is an important factor determining many of a substance's characteristics. Each substance will have its energy gap according to the gap between the valance and conduction bands. In this research, we employed Tauc's plots to determine the band gap, as shown in Figure 5. The plots were drawn by using $(\alpha hv)^n = k(hv - E_g)$ where α is absorptivity, hv is photon energy, k is constant, and $n=2$ for direct transition [22]. Here, $(\alpha hv)^2$ v/s hv is drawn so that $(\alpha hv)^2$ along the Y-axis and hv along the X-axis. The interception intern is called the E_g value after plotting the neat curve, taking tangent, and extrapolating to the X-axis. These values were found to be increased from 2.250 to 2.653 eV (X=0.02-0.08), as shown in Table 2.

Table 2. Band gap values of MnCu ferrite.

Composition (X)	0.02	0.04	0.06	0.08
E_g values (eV)	2.250	2.280	2.594	2.653

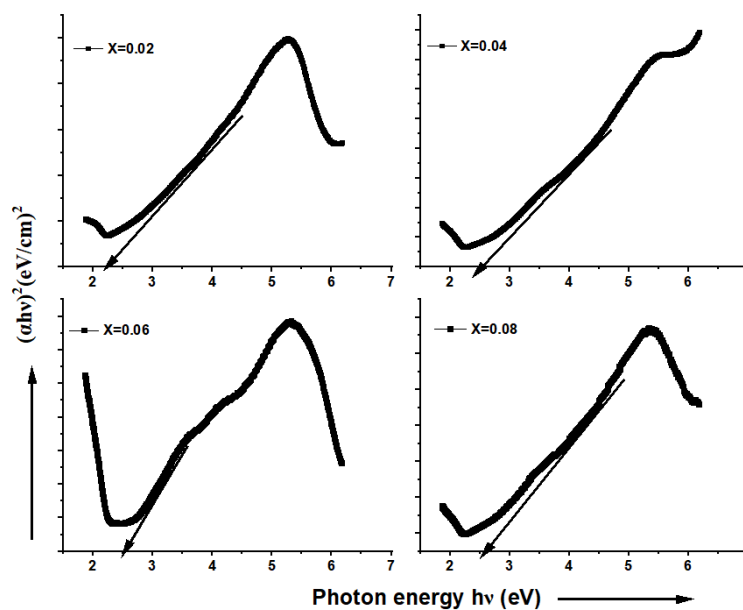


Figure 5. Tauc's plots of MCF NPs.

The FTIR spectra of MCF (X=0.02-0.08) have been recorded in the wavenumber range 4000 to 400 cm^{-1} , as shown in Figure 6. These spectra showed the presence of metal oxide bonds (M-O) such as Mn-O and Cu-O. At the wavenumber, 1384 cm^{-1} absorption peak was

noticed, indicating that bending vibrations were noticed for all compositions, and the predominant absorption peak was observed at the wavenumber 1641 cm^{-1} , indicating that stretched vibrations are confirmed in the compound due to the presence of H_2O molecules and O-H bonds exhibited the stretched vibrations at 3448 cm^{-1} . The FTIR spectra of MCF are shown in Figure 6. The absorption spectra are shown in Figure 7. The magnetization vs magnetic field (M–H) loops (Figure 8) can generally be used to explain the soft ferromagnetic character of the ferrite system due to their low coercivity and area covered. At room temperature (300 K), the samples were analyzed with a vibrating sample magnetometer to determine the ferromagnetic nature of the MCF system.

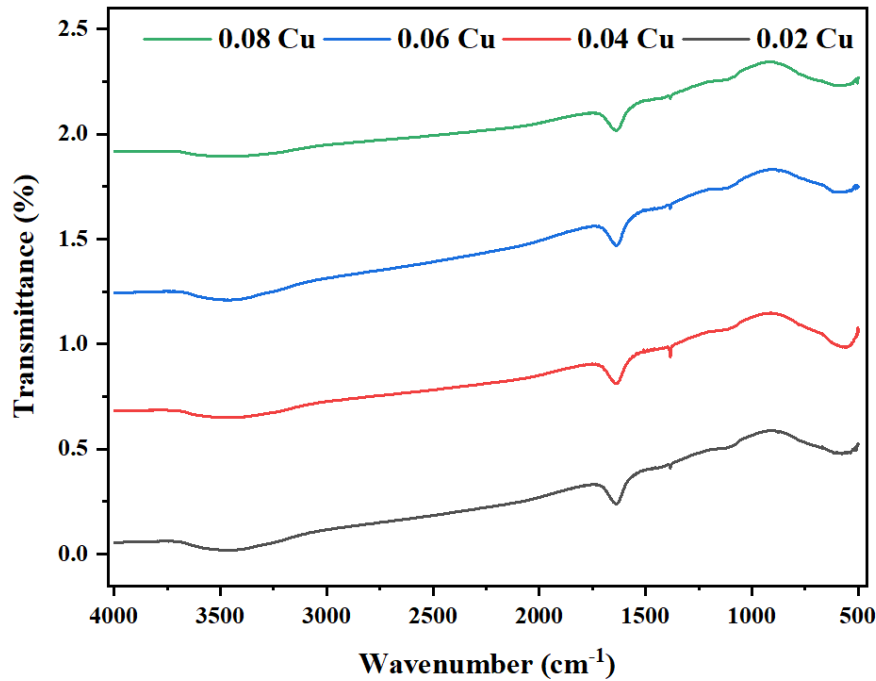


Figure 6. FTIR Spectra of MCF NPs(X=0.02-0.08).

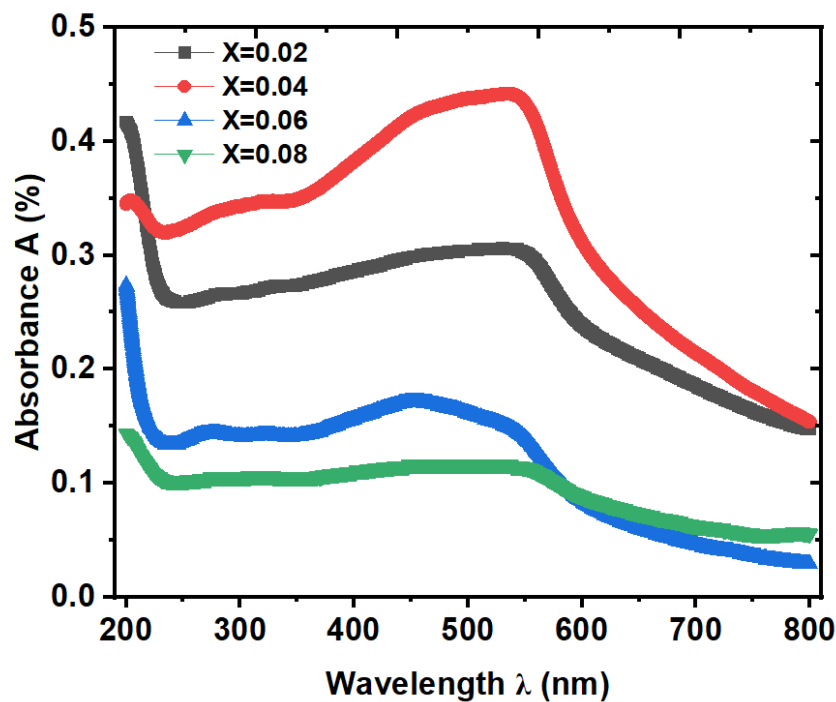


Figure 7. UV-visible absorption spectra of MCF nanoparticles.

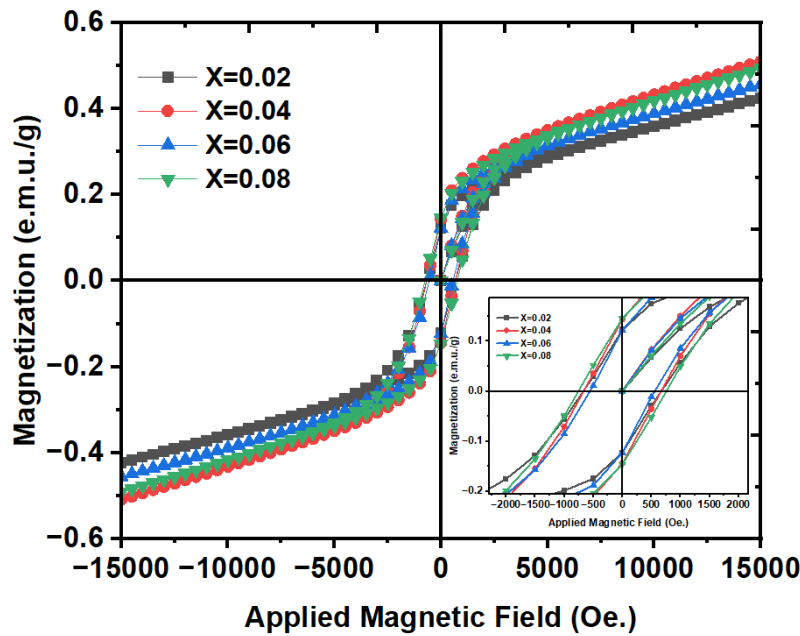


Figure 8. M–H loop of the MCF NPs.

Table 3. Magnetic parameters of the MCF NPs.

X	0.02	0.04	0.06	0.08
M_r (emu/g)	0.122	0.143	0.122	0.145
M_s (emu/g)	0.419	0.502	0.450	0.486
M_r/M_s	0.293	0.286	0.270	0.299
H_c (Oe)	672.134	667.214	553.924	757.546
K_1 (erg/cm ³)	293.365	349.391	260.044	383.610
n_B ($\mu\text{b/f.u}$)	0.017	0.020	0.018	0.020
ω_p (erg/cm ²)	0.201	0.217	0.1860	0.223
D_c (nm)	6.500	4.877	5.180	5.341

Figure 8 displays the generated hysteresis loops; a deep view of the hysteresis loop is displayed in the inset plot of Figure 8. It made it possible to track variations in the synthetic samples' coercivity. Conversely, the M–H loop was used to account for the magnetic parameters, which included remanence ratio (M_r/M_s), residual magnetization (M_r), hysteresis loop area (A), and saturation magnetization (M_s). These characteristics demonstrated the MCF NPs' soft ferromagnetic nature. Their tiny coercivity and retentivity values identified superparamagnetic NPs. As a result, it demonstrated how artificial materials are superparamagnetic. However, Table 3 has an evaluation and a summary of the magnetic parameters. As the Cu content increased from $y = 0.02, 0.04, 0.06,$ and 0.08 , the H_c increased from 672.134 to 757.546 G. It could be obtained because the crystallite size shrank from 71.4 to 53.6 nm. Thus, H_c and D have an inversely proportionate relationship; similar reports were found in the literature [23]. As the Cu content increased, the magnetic saturation (M_s) increased at $X=0.02, 0.04,$ and 0.08 but decreased at $X=0.06$. This trend is attributed to the trivalent rare earth element, which can influence the cation distribution and conversion of ferric ions into ferrous ions. Hence, the variation of magnetic moment and interaction variation occurs. This may occur because of a decrease in the magnetic exchange contact between the A and B sites [24, 25] or because the magnetic moment (n_B) decreases. This pattern for M_s can also be explained by an increase in the number of cations occupying lattice positions that are not magnetic. In the composition $X=0.02$ and 0.04 , the exchange interaction was increased in the Fe-O-Fe interactions so that the exchange length decreased between Fe and O. As reported in the literature, the cations distribution was mainly responsible for this kind of trend. In the case

of $X=0.6$, the magnetization and magnetic moment were decreased due to the increase in exchange length and thereby decreased exchange interactions. Moreover, in this sample, ferric conversion into ferrous ions occurs at both A and B sites. Commonly, the ferric ions will have a higher magnetic moment than ferrous ions. The conversion of Fe^{+3} to Fe^{+2} decreases the magnetization and magnetic moment. That is why $X=0.6$ showed the low M_s value 0.451 emu/g, the numerical squareness M_r/M_s values were varied from 0.2707-0.2995, if the squareness is less than 0.5 considered a multidomain magnetic structure and greater than 0.5 compound is single domain magnetic material. Hence, the NCF is a multidomain nanomagnetic material. The crystal anisotropy constant (K_1) is calculated, which gives the information about magnetization difference in hard (111) and soft (100) directions, and values vary from 260.044 to 383.610 erg/cm³. The magnitude of domain wall energy (ω_p) was noted for all compositions. The critical diameter D_c was noted to be 4.877-6.500 nm. Figure 9 shows the variation of the dielectric constant of the real part of the impedance (ϵ') and dielectric loss of the imaginary part of impedance (ϵ'') with respect to the applied frequency. We noticed that at a lower frequency, higher ϵ' and ϵ'' and as the frequency increases then both ϵ' and ϵ'' have been decreased. Koop's double layer theory reported the main reason for higher values of real part ϵ' in dielectric structure [26].

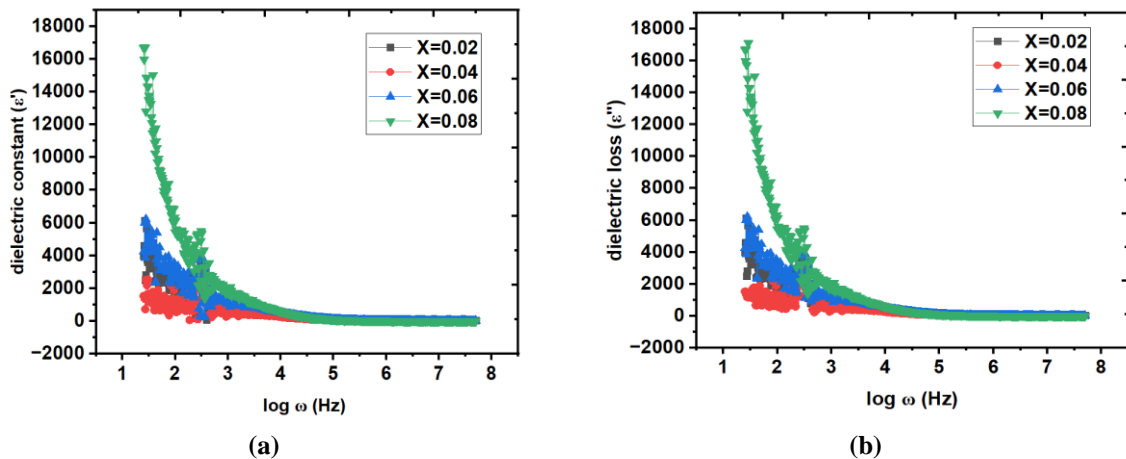


Figure 9. (a) Dielectric constant; (b) dielectric loss of $Mn_{1-x}Cu_xFe_2O_4$ NPs.

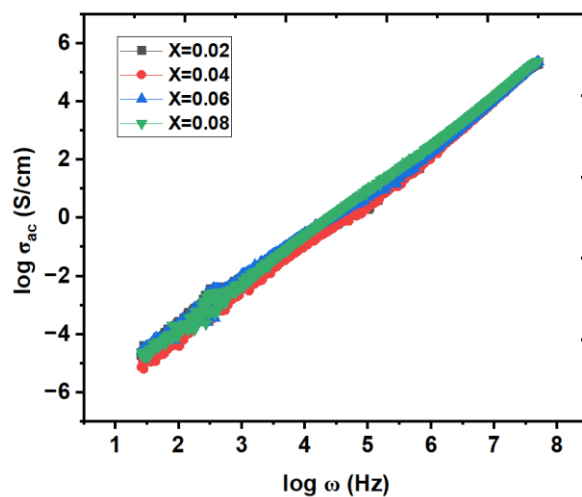


Figure 10. Frequency-dependent AC electrical conductivity of $Mn_{1-x}Cu_xFe_2O_4$.

Maxwell-Wagner's polarization [27] usually shows an effect at less than 100 Hz, achieving the piling-up nature of space charges at the grain boundary interface. This is also termed electrode polarization. The compositional variations of the real part and imaginary part

of impedance have been shown in Figure 9. The ϵ' value for $X=0.02$ to 0.04 has decreased from 184 to 179.011, and in the case of $X=0.06-0.08$ composition, the trend decreased from 428.737 to 354.081. Corresponding to the dielectric constant, the dielectric loss was higher at lower values of the dielectric constant and vice versa; hence, this MCF is referred to as loss dielectric materials. In this case, some data points were not considered due to the moisture content, defects, etc., reported in the literature. The AC electrical conductivity ($\log\sigma_{ac}$) increases with frequency, as seen in Figure 10. It is usual for conductivity to increase with frequency. At a lower dielectric loss, higher electrical conductivity, and higher dielectric loss, lower electrical conductivity is shown in Table 4. However, the ac-conductivity is rising due to the rise in dielectric loss. As frequency and composition increase, so does the AC electrical conductivity, as seen in Figure 10. A common behavior is an increase in conductivity with frequency.

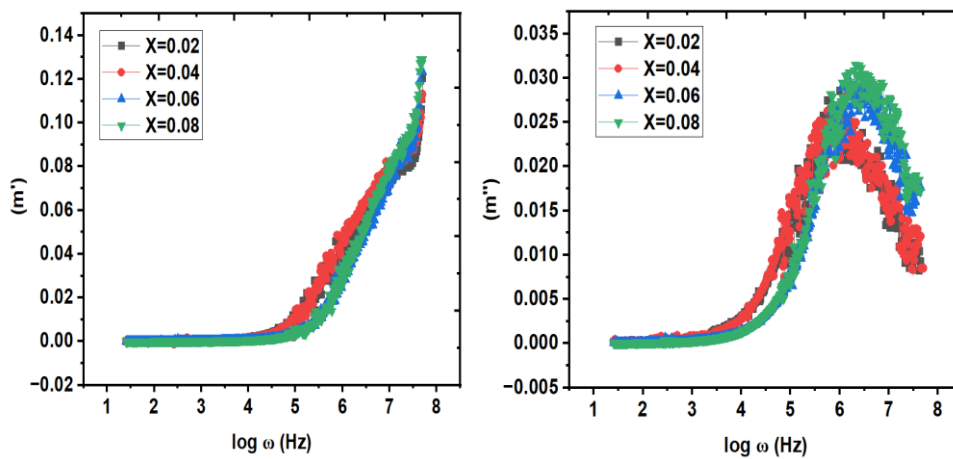


Figure 11. $\log \omega$ versus m' and m'' plots of $Mn_{1-x}Cu_xFe_2O_4$ NPs at $x=0.02, 0.04, 0.06$ and 0.08 .

Table 4. Dielectric data of MCF nanoparticles of $Mn_{1-x}Cu_xFe_2O_4$ NPs.

X	ϵ'	ϵ''	$\log\sigma_{ac}$ (s/m)
0.02	184	1161862	-1.113
0.04	179.011	112588	-1.202
0.06	428.737	2696539	-0.823
0.08	354.081	2226989	-0.906

$m^* = m' + jm''$, where $m' = \epsilon'/(\epsilon'^2 + \epsilon''^2)$ (real component) and $m'' = \epsilon''/(\epsilon'^2 + \epsilon''^2)$ (imaginary part), represents the complex dielectric modulus. The dielectric modulus formalism provides a clear understanding of the dielectric relaxation and polarisation mechanism, which includes space charge short- and long-range polarisation [28]. The fluctuation of m' and m'' with $\log \omega$ plot was explained as a function of composition in the example of $Mn_{1-x}Cu_xFe_2O_4$ NPs. Space charge polarisation will arise because, at lower frequencies, the charge carriers actively react to the input electric field frequency, as demonstrated by the compositions of $Mn_{1-x}Cu_xFe_2O_4$ NPs, which revealed zeros for m' and m'' . The charges can travel farther as a result. At this point, an inadequate state of strength to regulate the motion of charges via angular frequency may arise. Additionally, the restoring force will be relatively small in the event of low-frequency charges. These factors led to the m' and m'' of the contents of $x = 0.02, 0.04, 0.06$, and 0.08 acquiring zero value. Because of the charges' greater mobility over shorter distances, the m' and m'' values gradually increased as the angular frequency increased. M' mostly showed the significant relaxations $\log \omega = 7$ against $\log \omega$ graphs. The charges accumulated at the grain boundary interface, forming these relaxations. Because of this, m' maximum values will be found. Furthermore, only a small number of relaxations were seen at

frequencies lower than $\log \omega = 7$. However, for the contents of $x = 0.02, 0.04, 0.06,$ and $0.08,$ the m'' vs. $\log \omega$ plot (Figure 11) similarly showed the relaxations beyond $\log \omega = 6$.

The components of this relaxation are referred to as the high and low angular frequency areas. The charge carriers' short- and long-range mobilities were linked to the low- and high-frequency areas, respectively. Charges have the ability to move across extended distances due to their long-range mobility [29]. As a result, long-range polarisation will also grow, resulting in the evolution of the long-range hopping conduction mechanism [30]. The charge carriers will be significantly activated within the long-range polarisation area. Similarly, the charges' short-range mobility inside the high-frequency band demonstrated that they are limited in their range of motion. As documented in the literature, this resulted from restricting charges to the potential well. Consequently, the process of short-range polarisation will be produced, which may lead to the creation of a short-range hopping conduction mechanism [31].

Polycrystalline material studies using impedance spectroscopy have long been known to yield thorough insights into the kinetics of relaxation, electrical conduction mechanism, and space charge polarization [32, 33]. Here, it was established that grains and grain boundaries play a part in the electrical conduction mechanism. The complex impedance (Z^*) parameter was considered in light of this investigation. The actual part Z' and the imagined part Z'' were considered to be included in Z^* . The impedance spectra of $Mn_{1-x}Cu_xFe_2O_4$ NPs at $x = 0.02, 0.04, 0.06,$ and 0.08 are displayed in Figure 12.

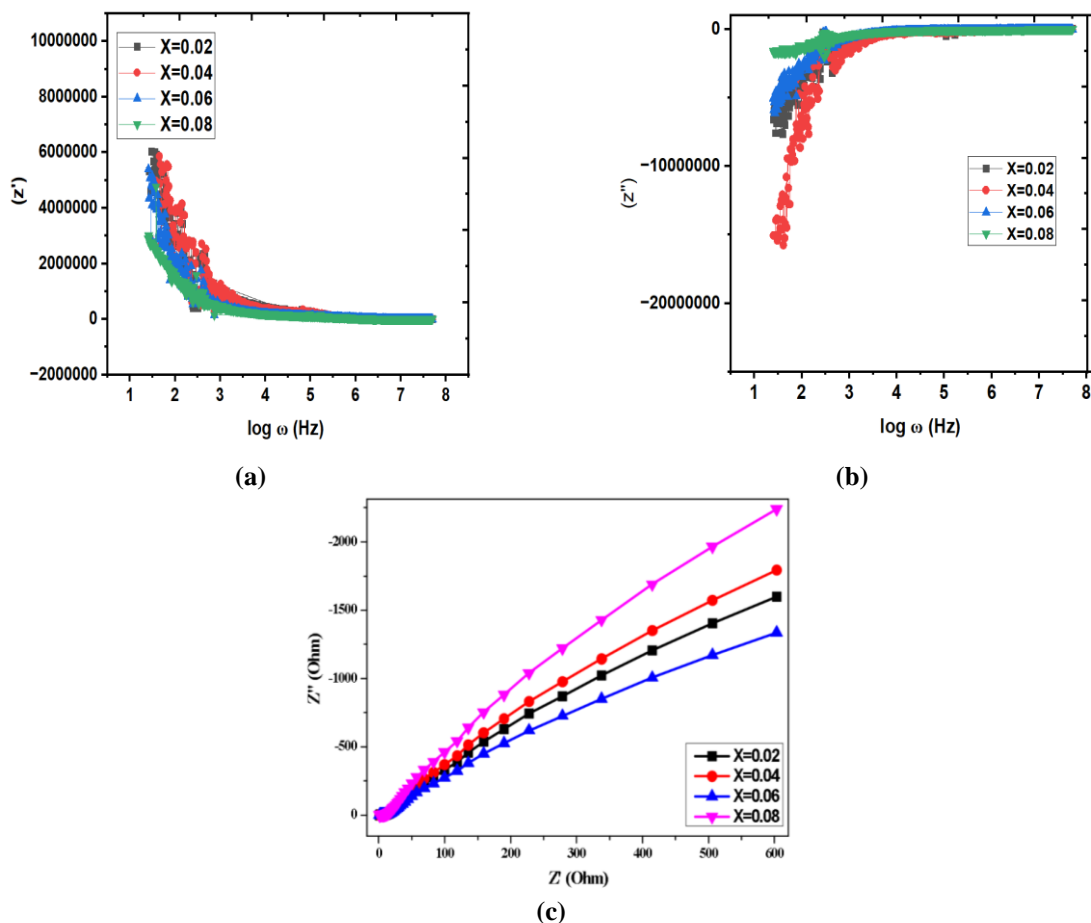


Figure 12. (a) \log frequency vs Z' ; (b) \log frequency vs Z'' ; (c) Z' vs Z'' of $Mn_{1-x}Cu_xFe_2O_4$ NPs.

This verifies that the $x = 0.8$ content spectra shift towards the y-axis. It demonstrates that, compared to other contents ($x = 0.02, 0.04,$ and 0.06), NPs with an $x = 0.8$ content exhibit the least resistance and the highest capacitance [34,35]. The frequency and Z' and Z'' of Mn_{1-x}

$x\text{Cu}_x\text{Fe}_2\text{O}_4$ nanoparticle was represented in Figure 12. It was seen from Figure 12 that the Z' had a high value at low $\log \omega$ values. The space charge effect was blamed for this. However, when the angular frequency increased, the Z' decreased. This demonstrated that there is insufficient time for the charges to align with the electric field's direction [36]. The Z' was reduced to low magnitude for very high $\log \omega$ values, indicating a decrease in the charges' reaction to the applied field. Furthermore, relaxations were executed at lower frequencies in certain compositions. According to Rahman *et al.*, these were caused by variations in grain size, flaws, moisture, strain, etc. Comparing the Z' of the $\text{Mn}_{1-x}\text{Cu}_x\text{Fe}_2\text{O}_4$ nanoparticle to the other content ($x = 0.02, 0.04$ and 0.06), the Z' for $x = 0.08$ content showed an almost growing trend.

Elevated values at reduced $\log \omega$ are displayed in the $Z'' - \log \omega$ plots of the contents of $x = 0.02, 0.04, 0.06$, and 0.08 (Figure 12). This occurred due to the polarisation effect of the electrode. Z'' grew up to $\log \omega > 3.241$ with an increase in $\log \omega$. All $\text{Mn}_{1-x}\text{Cu}_x\text{Fe}_2\text{O}_4$ nanoparticle concentrations demonstrated a declining trend of Z'' beyond this value. This report verified that relaxations were observed in the $\text{Mn}_{1-x}\text{Cu}_x\text{Fe}_2\text{O}_4$ nanoparticle compositions. These relaxations resulted from the oscillating electric dipole frequency and input field frequency matching. The declining trend of Z'' was seen upon relaxing. This tendency was observed due to charge carriers being released, which can occur due to a drop in potential barrier height, as documented in the literature [37].

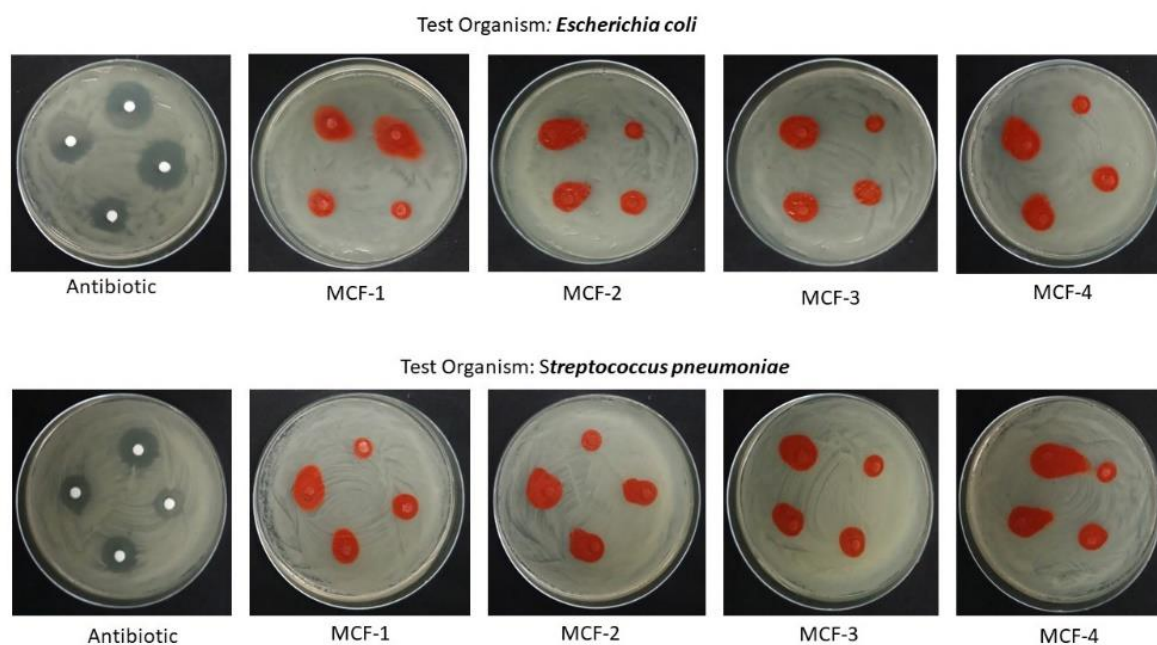


Figure 13. Antibacterial activity of chemically synthesized $\text{Mn}_{1-x}\text{Cu}_x\text{Fe}_2\text{O}_4$ against *Escherichia coli* and *Streptococcus pneumoniae* by disc diffusion method.

The disc diffusion method was used to test the antibacterial efficacy. A stock solution of 100 mg/mL was prepared by dissolving 0.1 g of extract into 100 mL of each of the solvents used to prepare the extract: distilled water and 100% ethanol. Then, extract concentrations of 5, 10, 20, and 30 mg/mL were obtained by diluting the stock solution. 20 μL of each dilution were impregnated onto sterile, 6 mm disc blanks. The extract was spotted in increments of 5 μL on both sides of the discs, with drying time in between [38, 39] to ensure even impregnation. Distilled water and ethanol-loaded discs served as negative controls for the aqueous and methanolic extracts, respectively. Each disc was fully dried out before being placed on the bacterial lawn. The discs' antibacterial efficacy was evaluated by measuring the diameter of the

enclosing inhibition zone (IZ). Three separate tests were performed. The antibacterial activity was quantified by measuring the average zone of inhibition in diameters (mm) that the leaf extract produced [40,41]. The antibacterial activity of $Mn_{1-x}Cu_xFe_2O_4$ was determined by the disc diffusion method. The present study evaluated the effect of different concentrations of chemically synthesized $Mn_{1-x}Cu_xFe_2O_4$ (MCF-1 to MCF-4) on *Escherichia coli* and *Staphylococcus aureus* [42,43]. This investigation showed *Escherichia coli* and *Streptococcus pneumoniae* methanolic extracts (Table 5). Compared to other extracts, the methanolic extract of *Streptococcus pneumoniae*, *Escherichia coli*, showed promising antifungal activity. Its diameter was 9 mm and 8 mm, and its MCF values ranged from 5 to 30 $\mu\text{g/ml}$. The effect of different concentrations of $Mn_{1-x}Cu_xFe_2O_4$ (5 to 30 $\mu\text{g/mL}$) synthesized by methanolic extract was evaluated for antibacterial activity on *Escherichia coli*, *Streptococcus pneumoniae* [44,45]. Differences in the physiology and structure of the various bacterial species may cause the observed variation in antibacterial activity.

Table 5. Using an agar disc diffusion approach, methanolic extracts inhibit the diameter of the infection zone on human pathogens.

Scientific name	concentration	MCF mg/ml	MCI mg/ml
<i>Streptococcus pneumoniae</i>	5	16.0	32.0
	10	17.3	33.2
	20	18.9	34.2
	30	19.29	35.9
<i>Escherichia coli</i>	5	17.1	31.2
	10	18.3	32.7
	20	19.75	33.45
	30	20.1	34.5

4. Conclusion

MCF NPs were synthesized using a hydrothermal technique. The synthesis of the cubic-spinel structure was represented in the XRD patterns. The structural characteristics were also assessed. Additionally, morphological characteristics were examined by FE-SEM, which revealed that the creation of nanofiber increased with Cu content. The FTIR analysis verified the cations' occupancy of the tetrahedral and octahedral sites. These findings also demonstrated the production of spinel ferrite. The $x = 0.02-0.08$ samples direct optical band gaps (E_g) demonstrated an increasing trend from 2.2504 to 2.6537 eV. As a result, sensor-based, photocatalytic, and optoelectronic devices can all be expressed using MCF nanofibers. Using M–H loops, the magnetic behavior was investigated. MCF NPs were manifested in the excellent antibacterial mechanism against pathogens *Escherichia coli*, and *Streptococcus pneumoniae*. The studies corroborate the multifunctionality of MCF NPs.

Funding

This research received no external funding.

Acknowledgments

The authors gratefully acknowledge the financial ‘Seed Grants’ support received from the GITAM (Deemed to be University) Ref: F. No. 2022/0187, date:02-05-2023.

Conflicts of Interest

The authors declare that we have no conflicts of interest.

References

1. Ma, H.; Liu, C. A mini-review of ferrites-based photocatalyst on application of hydrogen production. *Front. Energy* **2021**, *15*, 621–630, <https://doi.org/10.1007/s11708-021-0761-0>.
2. Thakur, P.; Taneja, S.; Sindhu, D.; Lüders, U.; Sharma, A.; Ravelo, B.; Thakur, A. Manganese Zinc Ferrites: a Short Review on Synthesis and Characterization. *J. Supercond. Nov. Magn.* **2020**, *33*, 1569–1584, <https://doi.org/10.1007/s10948-020-05489-z>.
3. Kakati, S.; Rendale, M.K.; Mathad, S.N. Synthesis, Characterization, and Applications of CoFe_2O_4 and $\text{M-CoFe}_2\text{O}_4$ (M = Ni, Zn, Mg, Cd, Cu, RE) Ferrites: A Review. *Int. J. Self-Propagating High-Temp. Synth.* **2021**, *30*, 189–219, <https://doi.org/10.3103/S1061386221040038>.
4. Mazen, S.A.; Elsayed, H.M.; Abu-Elsaad, N.I. Effect of divalent metal ions substitution on structural and magnetic properties of $\text{Li}_{0.25}\text{Mn}_{0.5-x}\text{M}_x\text{Fe}_{2.25}\text{O}_4$ (M = Co^{2+} , Ni^{2+} , Cu^{2+}) spinel ferrites. *Mater. Chem. Phys.* **2020**, *256*, 123676, <https://doi.org/10.1016/j.matchemphys.2020.123676>.
5. Abdellatif, M.H.; El-Komy, G.M.; Azab, A.A.; Moustafa, A.M.; Salerno, M. Crystal field deformation by Ce^{3+} doping in spinel Mn-Cr ferrite. *J. Magn. Magn. Mater.* **2020**, *502*, 166517, <https://doi.org/10.1016/j.jmmm.2020.166517>.
6. Patil, B.B. A review: Influence of divalent, trivalent, rare earth and additives ions on Ni–Cu–Zn ferrites. *J. Indian Chem. Soc.* **2023**, *100*, 100811, <https://doi.org/10.1016/j.jics.2022.100811>.
7. Dehghani Dastjerdi, O.; Shokrollahi, H.; Mirshekari, S. A review of synthesis, characterization, and magnetic properties of soft spinel ferrites. *Inorg. Chem. Commun.* **2023**, *153*, 110797, <https://doi.org/10.1016/j.inoche.2023.110797>.
8. Patil, K.; Phadke, S.; Mishra, A. A study of structural and dielectric properties of Zn^{2+} doped MnFe_2O_4 and NiFe_2O_4 spinel ferrites. *Mater. Today: Proc.* **2021**, *46*, 2226–2228, <https://doi.org/10.1016/j.matpr.2021.03.392>.
9. Hossain, M.D.; Hossain, M.A.; Sikder, S.S. Hysteresis loop properties of rare earth doped spinel ferrites: A review. *J. Magn. Magn. Mater.* **2022**, *564*, 170095, <https://doi.org/10.1016/j.jmmm.2022.170095>.
10. Nag, A.; Bose, R.S.C.; Manojkumar, A.; Venu, K.S.; Singh, H. Influence of doping on magnetic and electromagnetic properties of spinel ferrites. *Ceram. Int.* **2023**, *49*, 33099–33110, <https://doi.org/10.1016/j.ceramint.2023.08.011>.
11. El Abboubi, M.; San, S.E. Integration of spinel ferrite magnetic nanoparticles into organic solar cells: a review. *Mater. Sci. Eng. B* **2023**, *294*, 116512, <https://doi.org/10.1016/j.mseb.2023.116512>.
12. Zahid, M.; Khan, H.M.; Zeewaqar Manzoor, M.; Ejaz Ahmed, H.; Akhter, T.; Alshahrani, T.; Imran, M.; Assiri, M.A. Optimization of structural, dielectric, and magnetic properties of nanocrystalline copper doped spinel ferrites. *Mater. Sci. Eng. B* **2023**, *297*, 116739, <https://doi.org/10.1016/j.mseb.2023.116739>.
13. Salih, S.J.; Mahmood, W.M. Review on magnetic spinel ferrite (MFe_2O_4) nanoparticles: From synthesis to application. *Heliyon* **2023**, *9*, e16601, <https://doi.org/10.1016/j.heliyon.2023.e16601>.
14. Khan, N.; Irshad, I.; Almutairi, B.S.; Dahshan, A.; Hussain, A.; Tahir, M.B.; Ahmed, B.; Sagir, M. Sol-gel auto-combustion synthesis and characterization of Nd^{3+} doped $\text{Cu}_{0.5}\text{Co}_{0.5}\text{Fe}_{2-x}\text{Nd}_x\text{O}_4$ (x = 0.0, 0.1, 0.2, 0.3, 0.4, & 0.5) spinel ferrites. *Ceram. Int.* **2024**, *50*, 8594–8601, <https://doi.org/10.1016/j.ceramint.2023.08.037>.
15. Scherrer, P. Bestimmung der Größe und der inneren Struktur von Kolloidteilchen mittels Röntgenstrahlen. In *Nachrichten von der Gesellschaft der Wissenschaften zu Göttingen, Mathematisch-Physikalische Klasse*, **1918**; Volume 1918, 98–100.
16. Rahman, M.T.; Ramana C.V. Impedance spectroscopic characterization of gadolinium substituted cobalt ferrite ceramics. *J. Appl. Phys.* **2014**, *116*, 164108, <https://doi.org/10.1063/1.4896945>.
17. Peddigari, M.; Bharti, G.P.; Khare, A.; Dobbidi, P. Optical and dielectric studies on radio frequency sputtered Gd_2O_3 doped $\text{K}_{0.5}\text{Na}_{0.5}\text{NbO}_3$ thin films for nonlinear photonic and microwave tunable device applications. *J. Alloys Compd.* **2016**, *682*, 634–642, <https://doi.org/10.1016/j.jallcom.2016.05.061>.
18. Baharuddin, N.A.; Mohd Nazrul Aman, N.A.; Muchtar, A.; Somalu, M.R.; Abdul Samat, A.; Aznam, M.I. Structural, morphological, and electrochemical behavior of titanium-doped $\text{SrFe}_{1-x}\text{Ti}_x\text{O}_{3-\delta}$ (x = 0.1–0.5) perovskite as a cobalt-free solid oxide fuel cell cathode. *Ceram. Int.* **2019**, *45*, 12903–12909, <https://doi.org/10.1016/j.ceramint.2019.03.216>.
19. Shannon, R.D.; Prewitt, C.T. Revised values of effective ionic radii. *Acta Cryst.* **1970**, *26*, 1046–1048, <https://doi.org/10.1107/s0567740870003576>.

20. Baba Basha, D.; Suresh Kumar, N.; Chandra Babu Naidu, K.; Ranjith Kumar, G. Structural, electrical, and magnetic properties of nano $\text{Sr}_{1-x}\text{La}_x\text{Fe}_{12}\text{O}_{19}$ ($X = 0.2-0.8$). *Sci. Rep.* **2022**, *12*, 12723, <https://doi.org/10.1038/s41598-022-15250-2>.
21. Zhivulin, V.E.; Trofimov, E.A.; Zaitseva, O.V.; Sherstyuk, D.P.; Cherkasova, N.A.; Taskaev, S.V.; Vinnik, D.A.; Alekhina, Y.A.; Perov, N.S.; Naidu, K.C.B.; Elsaedy, H.I.; Khandaker, M.U.; Tishkevich, D.I.; Zubar, T.I.; Trukhanov, A.V.; Trukhanov, S.V. Preparation, phase stability, and magnetization behavior of high entropy hexaferrites. *iScience* **2023**, *26*, 107077, <https://doi.org/10.1016/j.isci.2023.107077>.
22. Samad, R.; Rather, M.u.D.; Asokan, K.; Want, B. Magneto-dielectric studies on multiferroic composites of Pr doped CoFe_2O_4 and Yb doped PbZrTiO_3 . *J. Alloys Compd.* **2018**, *744*, 453-462, <https://doi.org/10.1016/j.jallcom.2018.01.403>.
23. Naresh, U.; Kumar, R.J.; Naidu, K.C.B. Optical, magnetic and ferroelectric properties of $\text{Ba}_{0.2}\text{Cu}_{0.8-x}\text{La}_x\text{Fe}_2\text{O}_4$ ($x = 0.2-0.6$) nanoparticles. *Ceram. Int.* **2019**, *45*, 7515-7523, <https://doi.org/10.1016/j.ceramint.2019.01.044>.
24. Naresh, U.; Kumar, R.J.; Babu Naidu, K.C. Structural, morphological, optical, magnetic and ferroelectric properties of $\text{Ba}_{0.2}\text{La}_{0.8}\text{Fe}_2\text{O}_4$ nanofibers. *Biointerface Res. Appl. Chem.* **2019**, *9*, 4243-4247, <https://doi.org/10.33263/briac95.243247>.
25. El-Shater, R.E.; El Shimy, H.; Saafan, S.A.; Darwish, M.A.; Zhou, D.; Naidu, K.C.B.; Khandaker, M.U.; Mahmoud, Z.; Trukhanov, A.V.; Trukhanov, S.V.; Fakhry, F. Fabrication of doped ferrites and exploration of their structure and magnetic behavior. *Mater. Adv.* **2023**, *4*, 2794-2810, <https://doi.org/10.1039/d3ma00105a>.
26. Koops, C.G. On the Dispersion of Resistivity and Dielectric Constant of Some Semiconductors at Audiofrequencies. *Phys. Rev.* **1951**, *83*, 121, <https://doi.org/10.1103/physrev.83.121>.
27. Wagner, K.W. The Distribution of Relaxation Times in Typical Dielectrics. *Ann. Phys.* **1973**, *40*, 817-819.
28. Joshi, J.H.; Kanchan, D.K.; Joshi, M.J.; Jethva, H.O.; Parikh, K.D. Dielectric relaxation, complex impedance and modulus spectroscopic studies of mix phase rod like cobalt sulfide nanoparticles. *Mater. Res. Bull.* **2017**, *93*, 63-73, <https://doi.org/10.1016/j.materresbull.2017.04.013>.
29. Hang, B.T.; Van Dang, T.; Van Quy, N. $\text{Fe}_2\text{O}_3/\text{C}$ nanomaterials synthesized by microwave for energy storage applications. *Adv. Nat. Sci: Nanosci. Nanotechnol.* **2023**, *14*, 045016, <https://doi.org/10.1088/2043-6262/ad089f>.
30. Mansour, S.F.; Abdo, M.A.; Alwan, S.M. The role of Cr^{3+} ions substitution on structural, magnetic and dielectric modulus of manganese zinc nanoferrites. *Ceram. Int.* **2018**, *44*, 8035-8042, <https://doi.org/10.1016/j.ceramint.2018.01.244>.
31. Peddigari, M.; Sindam, B.; Raju, K.C.J.; Dobbidi, P. Optical and Microwave Dielectric Properties of Phase Pure $(\text{K}_{0.5}\text{Na}_{0.5})\text{NbO}_3$ Thin Films Deposited by RF Magnetron Sputtering. *J. Am. Ceram. Soc.* **2015**, *98*, 1444-1452, <https://doi.org/10.1111/jace.13502>.
32. Airimioaei, M.; Palamaru, M.-N.; Iordan, A.R.; Berthet, P.; Decorse, C.; Curecheriu, L.; Mitoseriu, L. Structural Investigation and Functional Properties of $\text{Mg}_x\text{Ni}_{1-x}\text{Fe}_2\text{O}_4$ Ferrites. *J. Am. Ceram. Soc.* **2014**, *97*, 519-526, <https://doi.org/10.1111/jace.12683>.
33. Li, J.; Lan, X.-K.; Wang, F.; Fan, J.; Lu, W.-Z.; Lei, W. Impedance spectroscopy and dielectric properties of $\text{BaAl}_{(2-2x)}(\text{Zn}_{0.5}\text{Ti}_{0.5})_{2x}\text{O}_4$ ceramics. *Ceram. Int.* **2020**, *46*, 1830-1835, <https://doi.org/10.1016/j.ceramint.2019.09.159>.
34. Das, A.; Dobbidi, P. Impedance Spectroscopy and ac Conductivity in $\text{Ba}_{0.5}\text{Sr}_{0.5}\text{TiO}_3\text{-Ca}_{10}(\text{PO}_4)_6(\text{OH})_2$ Ceramic Composites: An Electrical Approach to Unveil Biocomposites. *ACS Biomater. Sci. Eng.* **2021**, *7*, 2296-2308, <https://doi.org/10.1021/acsbiomaterials.1c00009>.
35. Ravikiran, U.; Zacharias, E.; Rajashekhar, G.; Sarah, P. Impedance spectroscopy studies on samarium and sodium substituted strontium bismuth titanate (SBTi). *Ceram. Int.* **2019**, *45*, 15188-15198, <https://doi.org/10.1016/j.ceramint.2019.05.003>.
36. Mallikarjuna, A.; Ramesh, S.; Kumar, N.S.; Naidu, K.C.B.; Ratnam, K.V.; Manjunatha, H. Photocatalytic Activity, Negative AC-Electrical Conductivity, Dielectric Modulus, and Impedance Properties in 0.6 $(\text{Al}_{0.2}\text{La}_{0.8}\text{TiO}_3)$ + 0.4 (BiFeO_3) Nanocomposite. *Cryst. Res. Technol.* **2020**, *55*, 2000068, <https://doi.org/10.1002/crat.202000068>.
37. Naresh, U.; Kumar, R.J.; Naidu, K.C.B. Hydrothermal synthesis of barium copper ferrite nanoparticles: Nanofiber formation, optical, and magnetic properties. *Mater. Chem. Phys.* **2019**, *236*, 121807, <https://doi.org/10.1016/j.matchemphys.2019.121807>.

38. Bharathi, S.D.; Babu, D.R. Synthesis, characterization and antimicrobial activity of Manganese ferrite nanoparticles. *Mater. Sci. Eng. B* **2024**, *300*, 117051, <https://doi.org/10.1016/j.mseb.2023.117051>.
39. Parada, J.; Díaz, M.; Hermosilla, E.; Vera, J.; Tortella, G.; Seabra, A.B.; Quiroz, A.; Hormazábal, E.; Rubilar, O. Synthesis and Antibacterial Activity of Manganese-Ferrite/Silver Nanocomposite Combined with Two Essential Oils. *Nanomaterials* **2021**, *12*, 2137, <https://doi.org/10.3390/nano12132137>.
40. Yan, X.; He, B.; Liu, L.; Qu, G.; Shi, J.; Hu, L.; Jiang, G. Antibacterial mechanism of silver nanoparticles in *Pseudomonas aeruginosa*: proteomics approach. *Metallomics* **2018**, *10*, 557–564, <https://doi.org/10.1039/C7MT00328E>.
41. Babukutty, B.; Ponnamma, D.; Nair, S.S.; Jose, J.; Bhat, S.G.; Thomas, S. Structural, magnetic and antibacterial properties of manganese-substituted magnetite ferrofluids. *Int. J. Miner. Metall. Mater.* **2023**, *30*, 1417–1426, <https://doi.org/10.1007/s12613-022-2594-1>.
42. Yuliantika, D.; Taufiq, A.; Putra, E.G.R. Hierarchical structure and antibacterial activity of olive oil based MZFe₂O₄ ferrofluids. *J. Phys.: Conf. Ser.* **2020**, *1436*, 012145, <https://doi.org/10.1088/1742-6596/1436/1/012145>.
43. Ansari, M.A.; Baykal, A.; Asiri, S.; Rehman, S. Synthesis and Characterization of Antibacterial Activity of Spinel Chromium-Substituted Copper Ferrite Nanoparticles for Biomedical Application. *J. Inorg. Organomet. Polym. Mater.* **2018**, *28*, 2316–2327, <https://doi.org/10.1007/s10904-018-0889-5>.
44. He, Q.; Liu, J.; Liang, J.; Huang, C.; Li, W. Synthesis and Antibacterial Activity of Magnetic MnFe₂O₄/Ag Composite Particles. *Nanosci. Nanotechnol. Lett.* **2014**, *6*, 385–391, <https://doi.org/10.1166/nnl.2014.1774>.
45. Lagashetty, A.; Pattar, A.; Ganiger, S.K. Synthesis, characterization and antibacterial study of Ag doped magnesium ferrite nanocomposite. *Heliyon* **2019**, *5*, e01760, <https://doi.org/10.1016/j.heliyon.2019.e01760>.